Thermoelectrokinetic instability and salt superconcentration near permselective electric membranes

E. N. Kalaydin,[1,2] N. Yu. Ganchenko,[2] G. S. Ganchenko,[3] N. V. Nikitin,[4] and E. A. Demekhin[1,3,4,*]

[1]*Department of Mathematics and Informatics, Financial University, Krasnodar 350051, Russian Federation*

[2]*Department of Mathematical and Computer Methods, Kuban State University, Krasnodar 350040, Russian Federation*

[3]*Laboratory of Micro- and Nanoscale Electro- and Hydrodynamics, Financial University, Krasnodar 350051, Russian Federation*

[4]*Laboratory of General Aeromechanics, Institute of Mechanics, Moscow State University, Moscow 119192, Russian Federation*

(Received 25 July 2017; published 14 November 2017)

A sophisticated type of electrohydrodynamic instability, the thermoelectrokinetic instability, in an electrolyte solution near ion-selective surfaces in an external electric field was discovered and investigated theoretically. The investigation used parallel computing on the SKIF MSU Lomonosov supercomputer and it was based on the direct numerical simulation of the Nernst-Planck-Poisson-Navier-Stokes system, along with the energy equation and corresponding boundary conditions. Although the physical mechanism of the instability is connected with Joule heating, it dramatically differs from the well-known Raleigh-Bénard convection: The instability is caused by nonuniformity of the electric current and electric conductivity and, in contrast to the Raleigh-Bénard instability, it occurs when the heating is from above. The thermoelectrokinetic instability prevails in long microchannels and a good enough thermal insulation of the system and it can be an additional factor for the overlimiting current mode. Initial unstable small random disturbances of the unknowns evolve towards rather unusual coherent structures. For the cation-exchange membranes, the salt concentration was eventually localized in long narrow fingers that are similar to stalactites and that stretched from the anode in the direction of the cathode. Outside the stalactites, the salt concentration was practically zero, while inside the stalactites it could reach hundreds from the initial concentration. Consequently, it is possible to talk about its superconcentration. The electric current propagates in a narrow needle along the stalactite with maximal electric conductivity and this gives rise to Joule heating in this region. The space charge forms crownlike micropatterns near the cathode. Note that the regime of chaotic motion that is characteristic of the electrokinetic instability was not observed for the thermoelectrokinetic instability.

DOI: 10.1103/PhysRevFluids.2.114201

I. INTRODUCTION

Ion-selective membranes are widely used in many engineering applications such as water desalination, fuel cells, protein preconcentration, and electrodeposition [1–12]. The operational efficiency of a conducting ion-selective membrane is characterized by its voltage-current (VC) curve. As depicted in Fig. 1, a typical VC curve consists of three distinct regimes: a low-current Ohmic regime, a plateau-limiting regime, and an overlimiting current regime. While the first regime could be explained by the classical theory of concentration polarization [13,14] and the limiting regime was theoretically described by Rubinstein and Shtilman [15], for a long time the mechanism for the third regime was unclear. In fact, it is now known that several physical mechanisms may be responsible for the overlimiting regime (see [3,16–21] and Fig. 2). For a long time, water splitting

*edemekhi@gmail.com

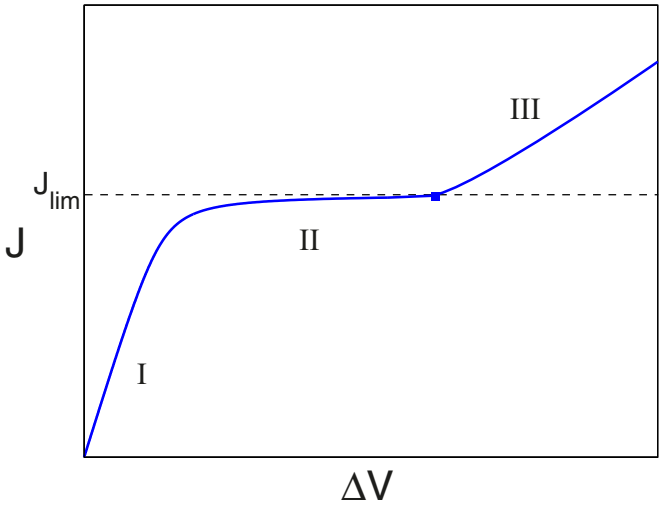

FIG. 1. Sketch of a typical VC curve of a permselective membrane. Labels I, II, and III correspond to the underlimiting, limiting, and overlimiting regimes.

was considered to be the only reason for the overlimiting regimes, especially because it is enhanced by the Kharkats effect [22]. The effect is determined by the fact that additional ions of dissociated water attract ions of salt and the salt ions' flux increases through the membrane. In this way, the sum of the electric current through the system becomes larger than the sum of the current due to ions of salt and water ions separately.

The second physical mechanism is connected with the fact that only a few real interfaces are molecularly smooth and homogeneous. Typically, the surface is rough and patchy on the microscale level due to the molecular structure, manufacturing technology, and so on. The membrane surface is covered with nonconductive patches and microroughness, with a characteristic size of inhomogeneity from microns to hundreds of microns [18,23–26]. These inhomogeneities create a nonuniform charge distribution, tangential electric field, and Coulomb force along the membrane surface and hence give rise to the Dukhin-Mischuk microvortex mechanism of overlimiting current. Note that inhomogeneity can be also formed by hydrophobic patches on the surface [27,28].

Rubinstein and Zaltzman [29] discovered a type of electrohydrodynamic instability that is caused by an electro-osmotic slip at the border of the extended space charge (ESC) region. In many cases, this is the most promising mechanism for the overlimiting current and it has been studied in [19,30–34]. This mechanism is termed electroconvective or electrokinetic instability. Historically, the term electroconvective instability has been used in several different contexts [35–38]. Therefore, in order not to be confused, we prefer to use the term electrokinetic instability or Rubinstein-Zaltzman

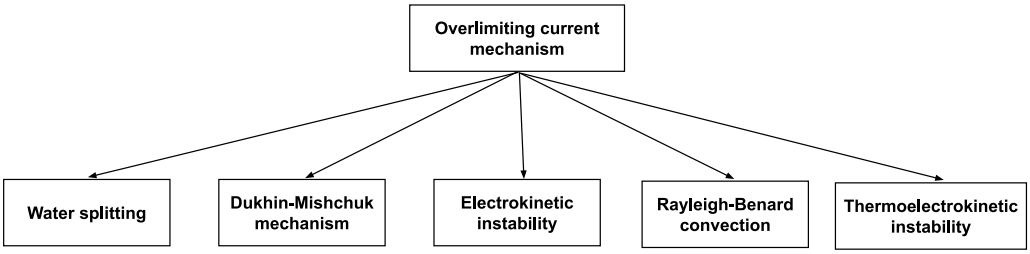

FIG. 2. Scheme of overlimiting current regime mechanisms.

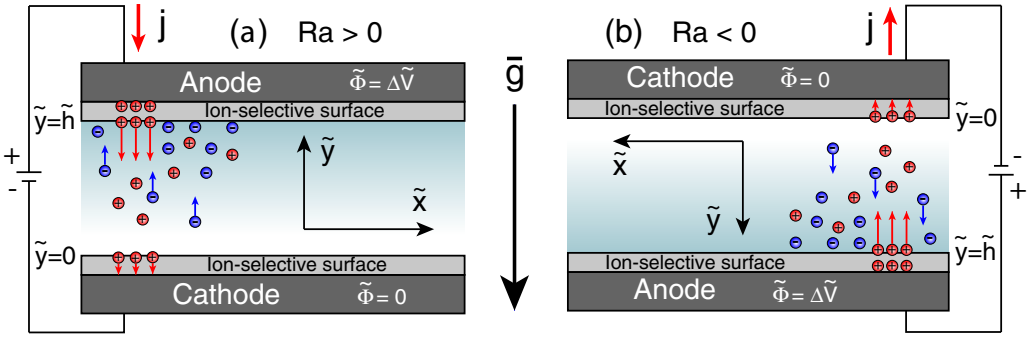

FIG. 3. Schematics of the system. The acceleration vector $\vec{\mathbf{g}}$ can be either codirected (Ra $<$ 0) or counterdirected (Ra $>$ 0) to the y axis.

microvortex instability. Instability caused by the interplay of the fluid density variation and the electrokinetic instability was studied in Refs. [39,40].

Usually, the thermal effects are neglected in theoretical and numerical analyses of instability near ion-selective surfaces. On the other hand, one of the major technological concerns in electrokinetically actuated microflows is Joule heating [41,42]. Rayleigh-Bénard convection caused by Joule heating is the fourth possible mechanism of the overlimiting mode [3]. At the present time, a comprehensive analysis of Rayleigh-Bénard instability applied to our problem is lacking.

Recently, a type of instability caused by Joule heating but different from the Rayleigh-Bénard convection was found theoretically [43]. This kind of instability was called thermoelectrokinetic instability. It is caused by nonuniformity of the electric current and electric conductivity and, in contrast to the Rayleigh-Bénard instability, it occurs when the heating is from above.

The present paper is a continuation of the investigation in [43]. Different results are the generalization of the numerical results of the linear stability of a quiescent equilibrium, the clarification of the instability mechanisms, the comprehensive nonlinear analysis based on the numerical simulation in two-dimensional (2D) and 3D cases, the study of 2D and 3D structures, which arise in the thermoelectroconvection mode, and the study of the influence of these structures on the voltage-current characteristic. The 3D calculations employ parallel computing.

The problem is described by a strongly nonlinearly coupled system of partial differential equations, the Nernst-Planck-Poisson-Stokes (NPPS) equations, along with the energy transfer equation. In addition to difficulties connected with strong nonlinearity, the solution of the system is complicated by a small parameter, the Debye number, at the highest derivatives. This problem can only be solved numerically. During the past few decades, direct numerical simulation (DNS) has been recognized as a powerful and reliable tool for studying many classical hydrodynamic stability problems. In particular, we have applied DNS for the electrokinetic instability [30–32].

II. FORMULATION OF THE PROBLEM

A symmetric binary electrolyte with a diffusivity of cations and anions $\tilde{D}$, dynamic viscosity $\tilde{\mu}$, and electric permittivity $\tilde{\varepsilon}$, and bounded by ideal, permselective ion-exchange membrane surfaces at $\tilde{y}=0$ and $\tilde{y}=\tilde{h}$ with a potential difference $\Delta\tilde{V}$ between these surfaces is treated (see Fig. 3). In this paper we consider the case of equal diffusivity of cations and anions. A solution of KCl can be used as such an electrolyte. In practice, diffusivities are not equal in most cases and an additional parameter $D=\tilde{D}^{+}/\tilde{D}^{-}$ appears in the system. The parameter varies from 0.5 to 5 for different solutions. It has been noted that for cation exchange membranes the increase of D leads to an increase of critical values of voltage as for nonequilibrium [19], equilibrium [44], and electrokinetic instabilities. At the same time, the behavior is qualitatively independent of D, so the research will be restricted to the case $D=1$. Joule heating generated by the passage of a current through the electrolyte is taken into

account. Terms with a tilde are used for the dimensional variables, as opposed to their dimensionless counterparts without a tilde. Here $\{\tilde{x},\tilde{y},\tilde{z}\}$ are the coordinates, where $\tilde{x}$ and $\tilde{z}$ are directed along the membrane surface and $\tilde{y}$ is normal to it.

The problem is described by the following NPPS equations, along with the energy equation: ion transport for the concentration of cations and anions $\tilde{c}^{\pm}$,

$$\frac{\partial \tilde{c}^{\pm}}{\partial \tilde{t}} + \tilde{\mathbf{u}} \cdot \nabla \tilde{c}^{\pm} = \tilde{D}\left[\pm \nabla \cdot \left(\frac{\tilde{F}}{\tilde{R}\tilde{T}} \tilde{c}^{\pm} \nabla \tilde{\Phi}\right) + \nabla^2 \tilde{c}^{\pm}\right]; \tag{1}$$

the Poisson equation for the electric potential $\tilde{\Phi}$,

$$\nabla \cdot (\tilde{\varepsilon} \nabla \tilde{\Phi}) = \tilde{F}(\tilde{c}^{-} - \tilde{c}^{+}); \tag{2}$$

the Stokes equations for a creeping flow,

$$\nabla \tilde{\Pi} = \tilde{\mu} \nabla^2 \tilde{\mathbf{u}} + \tilde{F} \nabla \tilde{\Phi} (\tilde{c}^{-} - \tilde{c}^{+}) + \tilde{g} \tilde{r}_0 \tilde{\beta} (\tilde{T} - \tilde{T}_0) \mathbf{e_y}, \quad \nabla \cdot \tilde{\mathbf{u}} = 0, \tag{3}$$

and the energy equation

$$\frac{\partial \tilde{T}}{\partial \tilde{t}} + \tilde{\mathbf{u}} \cdot \nabla \tilde{T} = \tilde{a} \nabla^2 \tilde{T} - \frac{\tilde{\mathbf{I}} \cdot \nabla \tilde{\Phi}}{\tilde{c}_p \tilde{r}_0}, \tag{4}$$

where $\tilde{F}$ is Faraday's constant, $\tilde{R}$ is the universal gas constant, $\tilde{T}$ and $\tilde{T}_0$ are the temperatures of the electrolyte and the environment, respectively, $\tilde{\varepsilon}$ is the electric permittivity, $\tilde{g}$ is the acceleration due to gravity, $\tilde{r}_0$ is the density, $\tilde{\beta}$ is the thermal expansion coefficient, $\tilde{c}_p$ is the specific heat capacity, and $\tilde{a}$ is the thermal diffusivity. In these equations, the 2D and 3D cases are treated; $\tilde{\mathbf{u}} = (\tilde{U},\tilde{V},\tilde{W})$ is the fluid velocity vector and $\tilde{\Pi}$ is the pressure.

Physically, an additional transport mechanism appears in the electrolyte with temperature differences: thermal diffusion (Soret effect). The effect was discovered in the 19th century [45], but it was not widely used, because it is secondary to others and suppressed by convection in macroscales. Recently, studies of thermal diffusion have begun in microscales, where this effect may be significant [46–48]. In most of the available work, the system was affected by the temperature difference and papers on the study of the Soret effect with Joule heating are lacking in the literature. This topic deserves special investigation and is beyond the scope of this paper, so we will neglect thermal diffusion further in the present article.

Equation (3) contains the term of buoyancy force in the Boussinesq approximation, where the unit vector $\mathbf{e_y}$ is directed along the y axis. The energy equation contains the source term that is associated with Joule heating of the electrolyte. The full electric current

$$\tilde{\mathbf{I}}_{\text{full}} = -\frac{\tilde{F}^2 \tilde{D}}{\tilde{R}\tilde{T}} (\tilde{c}^{+} + \tilde{c}^{-}) \nabla \tilde{\Phi} - \tilde{F} \tilde{D} \nabla (\tilde{c}^{+} - \tilde{c}^{-}) + \tilde{F} \tilde{\mathbf{u}} (\tilde{c}^{+} - \tilde{c}^{-})$$

is made up of contributions from the electrical conductivity, the diffusion of charge, and the convection of charge (see [14]). The first term is readily recognized as an expression of Ohm's law with the electrical conductivity $(\tilde{c}^{+} + \tilde{c}^{-})\tilde{F}^2 \tilde{D}/\tilde{R}\tilde{T}$. The convective term does not contribute to Joule heating and

$$\tilde{\mathbf{I}} = -\frac{\tilde{F}^2 \tilde{D}}{\tilde{R}\tilde{T}} (\tilde{c}^{+} + \tilde{c}^{-}) \nabla \tilde{\Phi} - \tilde{F} \tilde{D} \nabla (\tilde{c}^{+} - \tilde{c}^{-}) \tag{5}$$

has to be taken for the source term in (4).

This system of dimensional equations is complemented by the following boundary conditions (BCs): For $\tilde{y} = 0$,

$$\tilde{c}^{+} = \tilde{p}, \quad -\frac{\tilde{F}\tilde{c}^{-}}{\tilde{R}\tilde{T}} \frac{\partial \tilde{\Phi}}{\partial \tilde{y}} + \frac{\partial \tilde{c}^{-}}{\partial \tilde{y}} = 0, \quad \tilde{\Phi} = 0, \quad \tilde{\mathbf{u}} = \mathbf{0}, \quad -\frac{\partial \tilde{T}}{\partial \tilde{y}} + \frac{\tilde{\alpha}}{\tilde{\lambda}_T} (\tilde{T} - \tilde{T}_0) = 0, \tag{6}$$

and for $\tilde{y} = \tilde{h}$,

$$\tilde{c}^+ = \tilde{p}, \quad \frac{\tilde{F}\tilde{c}^-}{\tilde{R}\tilde{T}}\frac{\partial\tilde{\Phi}}{\partial\tilde{y}} - \frac{\partial\tilde{c}^-}{\partial\tilde{y}} = 0, \quad \tilde{\Phi} = \Delta\tilde{V}, \quad \tilde{\mathbf{u}} = \mathbf{0}, \quad \frac{\partial\tilde{T}}{\partial\tilde{y}} + \frac{\tilde{\alpha}}{\tilde{\lambda}_T}(\tilde{T} - \tilde{T}_0) = 0, \tag{7}$$

where $\tilde{\alpha}$ is the heat transfer coefficient and $\tilde{\lambda}_T$ is the thermal conductivity of the fluid. The first BC, prescribing an interface concentration equal to that of the fixed charges inside the membrane, is asymptotically valid for large $\tilde{p}$ and was introduced by Rubinstein (see, for example, Ref. [19]). This condition prevents the calculation of the complete solution within the porous membrane. The second BC indicates that there is no total flux for negative ions. The third condition is a fixed potential drop. In the fourth condition, the velocity vanishes at the rigid surface. The last condition corresponds to the mixed thermal BCs. The spatial domain is assumed to be infinitely large in the $\tilde{x}$ and $\tilde{z}$ directions and the boundedness of the solution as $\tilde{x},\tilde{z} \to \pm\infty$ is imposed as a boundary condition. This statement, but without thermal effects, was presented in [32].

To make the system dimensionless, the characteristic quantities are as follows: $\tilde{h}$ is the characteristic length, the distance between the membranes; $\tilde{h}^2/\tilde{D}$ is the characteristic time; $\tilde{\mu}$ is the dynamic viscosity; $\tilde{c}_\infty$ is the electrolyte concentration at $\tilde{t} = 0$ when there is no potential difference between the membranes and the ions distribution is uniform and electroneutral; and the thermic potential $\tilde{\Phi}_0 = \tilde{R}\tilde{T}_0/\tilde{F}$ is taken as the characteristic potential with $\tilde{T}_0 = 300$ K. The characteristic temperature difference can be obtained from the balance between Joule heating and the energy loss to the environment. To do this, the energy equation (4) for the 1D case

$$\tilde{a}\frac{d^2\tilde{T}}{d\tilde{y}^2} = \frac{\tilde{I}}{\tilde{c}_p\tilde{r}_0}\frac{d\tilde{\Phi}}{d\tilde{y}}$$

is integrated with respect to $\tilde{y}$ from 0 to $\tilde{h}$ and upon substituting the BCs (6) and (7) for the temperature, it turns into

$$\tilde{a}\frac{\tilde{\alpha}}{\tilde{\lambda}_T}[(\tilde{T} - \tilde{T}_0)|_{\tilde{y}=\tilde{h}} + (\tilde{T} - \tilde{T}_0)|_{\tilde{y}=0}] = -\int_0^{\tilde{h}} \frac{\tilde{I}}{\tilde{c}_p\tilde{r}_0}\frac{d\tilde{\Phi}}{d\tilde{y}}d\tilde{y}.$$

The characteristic temperature difference $\tilde{T}_{\mathrm{ch}} = \frac{\tilde{\Phi}_0\tilde{D}\tilde{F}\tilde{c}_\infty}{\tilde{a}\tilde{c}_p\tilde{r}_0}\frac{\tilde{\lambda}_T}{\tilde{\alpha}\tilde{h}}$ is found from the last relation.

Small deviations of the electrolyte temperature $\tilde{T}$ from the environmental temperature $\tilde{T}_0$ are considered. There is a dependence of the system parameters on the temperature.

First, the ion transport equations (1), the relation for the electric current (5), and BCs of no flux for negative ions, (6) and (7), contain terms $\tilde{F}/\tilde{R}\tilde{T}$. Our previous work [43] showed that for realistic values of the parameters this dependence does not affect the problem and can be neglected, $\tilde{F}/\tilde{R}\tilde{T} \approx \tilde{F}/\tilde{R}\tilde{T}_0$.

Second, the permittivity $\tilde{\varepsilon}$ is a function of the temperature. In [43] it was assumed to be a linear function of $\tilde{T}$; for aqueous solutions $\frac{1}{\tilde{\varepsilon}}\frac{\partial\tilde{\varepsilon}}{\partial\tilde{T}} = -4.6 \times 10^{-3}$ K^{-1} (see [49]). This dependence has to be taken into account in the Poisson equation (3) and it provides an additional term, namely,

$$\Lambda\nabla T \cdot \nabla\Phi,$$

where $\Lambda = \frac{1}{\tilde{\varepsilon}}\frac{\partial\tilde{\varepsilon}}{\partial\tilde{T}}\tilde{T}_{\mathrm{ch}}$.

The characteristic temperature, based on Joule heating, is $\tilde{T}_{\mathrm{ch}} = 0.1$–$1$ K and $|\Lambda| = (5 \times 10^{-4})$–$(5 \times 10^{-3})$. Keeping this term with nonzero Λ in the Poisson equation provides a weakly stabilizing effect (see Fig. 5 in [43]). In the present investigation, this term, and hence the dependence of $\tilde{\varepsilon}$ on $\tilde{T}$, is neglected. Note that the dependence $\tilde{\varepsilon}(\tilde{T})$ is important for some electrohydrodynamical problems (see, for example, [50,51]).

Third, the density dependence on the temperature gives rise to the buoyancy force in the Stokes equation (3). This dependence is crucial for our analysis.

Eventually, in the dimensionless formulation, the system (1)–(4) is

$$\frac{\partial c^{\pm}}{\partial t} + \mathbf{u}\cdot\nabla c^{\pm} = \pm\nabla\cdot(c^{\pm}\nabla\Phi) + \nabla^2 c^{\pm}, \tag{8}$$

$$\nabla^2\Phi = -\frac{\rho}{\nu^2}, \tag{9}$$

$$\nabla\Pi = \nabla^2\mathbf{u} - \frac{\varkappa}{\nu^2}\nabla\Phi\rho + \mathrm{Ra}T\mathbf{e}_{\mathbf{y}}, \quad \nabla\cdot\mathbf{u} = 0, \tag{10}$$

$$\mathrm{Le}\left(\frac{\partial T}{\partial t} + \mathbf{u}\cdot\nabla T\right) = \nabla^2 T - \mathrm{Bi}\mathbf{I}\cdot\nabla\Phi, \tag{11}$$

where

$$\mathbf{I} = -K\nabla\Phi - \nabla\rho, \quad K = c^{+} + c^{-}, \quad \rho = c^{+} - c^{-}. \tag{12}$$

Here the factor K physically means the dimensional salt concentration and electrical conductivity.

The BCs are as follows: For $y = 0$,

$$c^{+} = p, \quad -c^{-}\frac{\partial\Phi}{\partial y} + \frac{\partial c^{-}}{\partial y} = 0, \quad \Phi = 0, \tag{13}$$

$$\mathbf{u} = \mathbf{0}, \quad -\frac{\partial T}{\partial y} + \mathrm{Bi}T = 0, \tag{14}$$

and for $y = 1$,

$$c^{+} = p, \quad c^{-}\frac{\partial\Phi}{\partial y} - \frac{\partial c^{-}}{\partial y} = 0, \quad \Phi = \Delta V, \tag{15}$$

$$\mathbf{u} = \mathbf{0}, \quad \frac{\partial T}{\partial y} + \mathrm{Bi}T = 0, \tag{16}$$

where $T = (\tilde{T} - \tilde{T}_0)/\tilde{T}_{\mathrm{ch}}$. Adding initial conditions for the cations, anions, and temperature completes the system (8)–(15). These initial conditions arise from the following viewpoint: When there is no potential difference between the membranes, the distribution of ions is homogeneous and electroneutral and the initial temperature is equal to the environmental temperature. This corresponds to the conditions $c^{+} = c^{-} = 1$ and $T = 0$. Some kind of small perturbations should be superimposed on this distribution: For $t = 0$,

$$c^{+} = 1 + \hat{c}^{+}(x,z), \quad c^{-} = 1 + \hat{c}^{-}(x,z), \quad T = \hat{T}(x,z), \quad \hat{c}^{\pm} \ll 1. \tag{17}$$

The initial perturbations that are natural from the viewpoint of the experiment are considered. The so-called room perturbations, which determine the external low-amplitude and broadband white noise, are superimposed as

$$\hat{c}^{+} = \int_{-\infty}^{+\infty}\hat{p}(k)e^{-ikx}dx, \quad \hat{c}^{-} = \int_{-\infty}^{+\infty}\hat{n}(k)e^{-ikx}dx, \quad \hat{T} = \int_{-\infty}^{+\infty}\hat{G}(k)e^{-ikx}dx, \tag{18}$$

where $\hat{p}(-k) = \hat{p}^{\dagger}(k)$, $\hat{n}(-k) = \hat{n}^{\dagger}(k)$, and $\hat{G}(-k) = \hat{G}^{\dagger}(k)$, with a dagger denoting a complex-conjugate value.

In our case, the channel surface is permeable only by the cations and hence the electric current j is determined only by the flux of the positive ions. The characteristic electric current j at the membrane surface is referred to as the limiting current $j_{\mathrm{lim}} = 4$,

$$j = c^{+}\frac{\partial\Phi}{\partial y} + \frac{\partial c^{+}}{\partial y} \quad \text{for } y = 0. \tag{19}$$

It is also convenient to introduce the electric current averaged over the membrane surface $l_x \times l_z$ and over time S:

$$\langle j(t)\rangle = \frac{1}{l_x l_z}\int_0^{l_x}\int_0^{l_z} j(x,z,t)dx\,dz, \quad J = \lim_{S\to\infty}\frac{1}{S}\int_0^S \langle j\rangle dt. \tag{20}$$

The infinite spatial domain is changed to a large enough finite domain that has lengths $l_x = l_z = l$ in both spatial dimensions, with the corresponding wave number $k = 2\pi/l$. The condition that the solution be bounded as $x,z \to \infty$ is changed to the periodic BCs. The length of the domain l has to be large enough to make the solution independent of the domain size.

The problem is described by seven dimensionless parameters: ν is the dimensionless Debye length or Debye number, $\varkappa$ is a coupling coefficient between the hydrodynamics and the electrostatics (it is essential that the coupling coefficient depends only upon the physical properties of the electrolyte), ΔV is the potential drop between the membranes, Ra is the electrostatic Rayleigh number, Bi is the Biot number (characterizing the system's thermal insulation with respect to the environment), Le is the Lewis number, and p is the membrane interface concentration in the BCs (13) and (15):

$$\begin{aligned} \nu &= \frac{\tilde{\lambda}_D}{\tilde{h}}, \quad \varkappa = \frac{\tilde{\varepsilon}\tilde{\Phi}_0^2}{\tilde{\mu}\tilde{D}}, \quad \Delta V = \frac{\Delta\tilde{V}}{\tilde{\Phi}_0}, \\ \mathrm{Ra} &= \frac{\tilde{g}\tilde{\beta}\tilde{r}_0\tilde{T}_{ch}\tilde{h}^3}{\tilde{\mu}\tilde{D}} = \frac{\tilde{F}}{\tilde{a}}\frac{\tilde{g}\tilde{\beta}}{\tilde{c}_p}\frac{\tilde{\Phi}_0\tilde{c}_\infty\tilde{h}^2}{\tilde{\mu}}\frac{\tilde{\lambda}_T}{\tilde{\alpha}}, \\ \mathrm{Bi} &= \frac{\tilde{\alpha}\tilde{h}}{\tilde{\lambda}_T}, \quad \mathrm{Le} = \frac{\tilde{D}}{\tilde{a}}, \quad p = \frac{\tilde{p}}{\tilde{c}_\infty}, \end{aligned} \tag{21}$$

where $\tilde{\lambda}_D = \sqrt{\frac{\tilde{\varepsilon}\tilde{\Phi}_0}{\tilde{F}\tilde{c}_\infty}}$ is the Debye length. To give an idea of the values of these dimensionless numbers, typical dimensional values for an aquatic solution of KCl for normal conditions are taken to be $\tilde{\Phi}_0 = 0.025$ V, $\tilde{D} = 2\times10^{-9}$ m^2/s, $\tilde{\varepsilon} = 7\times10^{-10}$ C^{2}s^2/(kg m^3), $\tilde{r}_0 = 10^3$ kg/m^3, $\tilde{\beta} = 2.07\times10^{-4}$ K^{-1}, $\tilde{c}_p = 4182$ J/(kg K), $\tilde{a} = 1.53\times10^{-7}$ m^2/s, and $\tilde{\lambda}_T = 0.602$ W/(m K). The channel width varies in the range of micro- to macrosizes, $\tilde{h} = 0.1$ μm to 1 mm, and the bulk concentration of the electrolyte is about $\tilde{c}_\infty = 1$–10^3 mol/m^3. The heat transfer coefficient between the electrolyte and the environment $\tilde{\alpha}$ depends on many factors and for each particular case it should be determined experimentally. We assume that it changes within a window as $\tilde{\alpha} = 10^{-1} - 10^3$ W/(m^2 K). The characteristic temperature difference, based on Joule heating, is $\tilde{T}_{\mathrm{ch}} = 0.1$–1 K.

Note that the classical Rayleigh number R is defined as

$$R = \frac{\tilde{g}\tilde{\beta}\tilde{r}_0\tilde{T}_{\mathrm{ch}}\tilde{h}^3}{\tilde{\mu}\tilde{a}} \tag{22}$$

and hence is related to our Rayleigh number Ra as

$$R = \mathrm{Le}\,\mathrm{Ra}. \tag{23}$$

From the analysis of the previously mentioned dimensional values, it follows that the dimensionless parameters vary within the ranges $\nu = 10^{-6}$–10^{-2} [the Debye number is a small parameter, which makes the problem singular and forms a thin electric double layer (EDL) near the boundaries of the investigated domain, $y = 0$ and $y = 1$], $\varkappa = 0.05$–0.5, and $\mathrm{Ra} = 10^{-6}$–10^3. It is assumed that the other dimensionless parameters can be fixed as $p = 5$ (see [19,52]) and $\mathrm{Le} = 0.013$ (for water). We assume that Bi, $\varkappa$, and ν are fixed: $\mathrm{Bi} = 10^{-2}$, $\varkappa = 0.2$, and $\nu = 0.01$. Now the problem is described by the two most important parameters: Ra and ΔV.

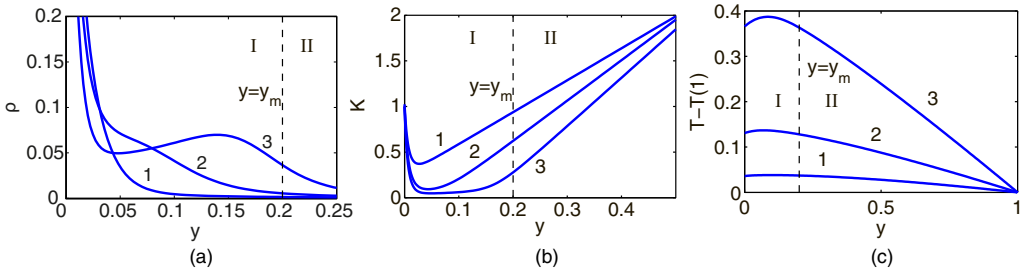

FIG. 4. One-dimensional steady solution for different ΔV, curves 1 for $\Delta V = 5$, curves 2 for $\Delta V = 10$, and curves 3 for $\Delta V = 20$. (a) charge density $\rho = c^+ - c^-$ near the membrane, (b) salt concentration $K = c^+ + c^-$, and (c) temperature $T - T(1)$, in I, the ESC region, and II, the electroneutral region; y_m stands for the boundary between I and II. The dot-dashed straight line stands for $y = y_m$ at the limiting regime 3.

III. RESULTS AND DISCUSSION

A. Underlimiting and limiting regimes and their stability

The system (8)–(17) always has a 1D steady-state solution $\partial/\partial t = \partial/\partial x = \partial/\partial z = 0$, which corresponds to a quiescent equilibrium of the system. For this solution, the system (8)–(17) can be transformed into

$$\rho\frac{d\Phi}{dy} + \frac{dK}{dy} = j, \quad K\frac{d\Phi}{dy} + \frac{d\rho}{dy} = j, \tag{24}$$

$$\nu^2\frac{d^2\Phi}{dy^2} = -\rho, \quad \frac{d^2T}{dy^2} + j\,\mathrm{Bi}\frac{d\Phi}{dy} = 0, \tag{25}$$

with the following BCs: For $y = 0$,

$$c^+ = p, \quad \Phi = 0, \quad -\frac{dT}{dy} + \mathrm{Bi}T = 0, \tag{26}$$

and for $y = 1$,

$$K + \rho = 2p, \quad \Phi = \Delta V, \quad \frac{dT}{dy} + \mathrm{Bi}T = 0. \tag{27}$$

Here j is the electric current density [see Eq. (19)], which for the 1D case is a constant of integration. Instead of the ion concentrations, it is convenient to introduce new variables, a salt concentration (which is the conductivity of the electrolyte) K and a charge density ρ. The liquid velocity is identically equal to zero, $U = V = W = 0$, and the buoyancy forces on the right-hand side of (10) are balanced by the pressure gradient and the electrostatic forces. In the absence of liquid motion, the ion transport is implemented by the following two mechanisms: diffusion and electromigration.

The electrostatic part of the system is decoupled from the thermal part and can be solved independently of the temperature field T; consequently, the analysis of equilibrium is equal to that conducted in [31]. The typical results of calculations are shown in Fig. 4. For the underlimiting currents, there is a thin EDL in a small vicinity, $O(\nu)$, of the charge-selective surface. For the limiting currents, the ESC region $0 < y < y_m$ is formed, while the region $y_m < y < 1$ is electroneutral. The ESC region is much thicker than the EDL, $O(\nu^{2/3}|\ln\nu|^{2/3}) < y_m < O(1)$ (see [19]), but is much thinner than the distance between the membranes, $y_m \ll 1$. For the 1D case, y_m is uniform along the membrane surface. For the 2D and 3D cases, the boundary of the ESC region gives a convenient value for describing the evolution. This boundary is a conventional value that we define by taking 5% of the maximal value of the space charge density in the ESC region. Temperature $T(y)$ reaches a maximum value in the ESC region, and in the electroneutral region it decreases almost linearly [see Fig. 4(c)].

A 1D equilibrium steady-state solution can lose its stability and be replaced by more complex 2D and 3D structures. Hence, the investigation is complemented by numerical calculation of the linear stability of the 1D quiescent solution with respect to the sinusoidal perturbations with a wave number k and a growth rate λ, $f = f_0(y) + \hat{f}(y)\exp(\lambda t + ikx)$, with $\hat{f} \to 0$ for $f = \{c^{\pm}, \Phi, V, T\}$. Without loss of generality, the perturbations are assumed to be two dimensional, $\partial/\partial z = 0$.

These perturbations trigger a hydrodynamic flow, so $\hat{V} \neq 0$. The subscript 0 indicates the mean 1D solution and a caret indicates the perturbations. Upon linearization of Eqs. (8)–(15) with respect to perturbations and omitting the subscript 0 in the mean solution, we get the system

$$\lambda\hat{K} + \frac{dK}{dy}\hat{V} = \frac{d}{dy}\left(\rho\frac{d\hat{\Phi}}{dy} + E\hat{\rho}\right) - k^2\rho\hat{\Phi} + \frac{d^2\hat{K}}{dy^2} - k^2\hat{K}, \tag{28}$$

$$\lambda\hat{\rho} + \frac{d\rho}{dy}\hat{V} = \frac{d}{dy}\left(K\frac{d\hat{\Phi}}{dy} + E\hat{K}\right) - k^2K\hat{\Phi} + \frac{d^2\hat{\rho}}{dy^2} - k^2\hat{\rho}, \tag{29}$$

$$\frac{d^2\hat{\Phi}}{dy^2} - k^2\hat{\Phi} = -\frac{\hat{\rho}}{\nu^2}, \tag{30}$$

$$\frac{d^4\hat{V}}{dy^4} - 2k^2\frac{d^2\hat{V}}{dy^2} + k^4\hat{V} = \frac{\varkappa}{\nu^2}k^2\left(\frac{d\rho}{dy}\hat{\Phi} - E\hat{\rho}\right) + k^2\mathrm{Ra}\hat{T}, \tag{31}$$

$$\mathrm{Le}\left(\lambda\hat{T} + \frac{dT}{dy}\hat{V}\right) = \frac{d^2\hat{T}}{dy^2} - k^2\hat{T} + \mathrm{Bi}\left(E\hat{j} + j\frac{d\hat{\Phi}}{dy}\right), \tag{32}$$

where $\hat{K} = \hat{c}^+ + \hat{c}^-$ and $\hat{\rho} = \hat{c}^+ - \hat{c}^-$ are, respectively, the perturbations of the salt concentration and the charge density and

$$j = c^+\frac{d\Phi}{dy} + \frac{dc^+}{dy}, \quad \hat{j} = \hat{K}E + K\frac{d\hat{\Phi}}{dy} + \frac{d\hat{\rho}}{dy} \quad \text{for } y = 0,$$

with the following BCs: For $y = 0$,

$$\hat{c}^+ = 0, \quad -\hat{c}^-E - c^-\frac{d\hat{\Phi}}{dy} + \frac{d\hat{c}^-}{dy} = 0, \tag{33}$$

$$\hat{\Phi} = 0, \quad \frac{d\hat{T}}{dy} - \mathrm{Bi}\hat{T} = 0, \quad \hat{V} = \frac{d\hat{V}}{dy} = 0, \tag{34}$$

and for $y = 1$,

$$\hat{c}^+ = 0, \quad -\hat{c}^-E - c^-\frac{d\hat{\Phi}}{dy} + \frac{d\hat{c}^-}{dy} = 0, \tag{35}$$

$$\hat{\Phi} = 0, \quad \frac{d\hat{T}}{dy} + \mathrm{Bi}\hat{T} = 0, \quad \hat{V} = \frac{d\hat{V}}{dy} = 0, \tag{36}$$

which is an eigenvalue problem for complex λ. If $\mathrm{Re}(\lambda) < 0$ for all the wave numbers k, then the 1D solution (24)–(27) is stable. If $\mathrm{Re}(\lambda) > 0$ for at least one k, then the 1D solution is unstable and it gives a bifurcation point of the system plus a transition point to the overlimiting currents.

Before the numerical investigation of the eigenvalue problem (28)–(36), it is instructive to clarify some important features of the thermoelectrokinetic instability. In our previous work [43] we derived

a thermo-osmotic slip correction to the galvano-osmotic slip velocity (see [19])

$$U_m = -\frac{\varkappa}{8}\Delta V^2 \frac{1}{j}\frac{\partial j}{\partial x} + \frac{3}{16}\nu^2 \Delta V^2 \mathrm{Ra}\frac{\partial}{\partial x}\left(\frac{T_m}{j}\right), \tag{37}$$

where the velocity U_m and temperature T_m are taken at the boundary $y = y_m$ of the ESC region. The flow is driven by the surface electric force (the first term) and the surface thermic force (the second term). At $\mathrm{Ra} = 0$, this relation coincides with the famous Rubinstein-Zaltzman formula [29]. The contribution of the second term is significant only for very large Rayleigh numbers $\mathrm{Ra} = O(1/\nu^2)$ and for realistic conditions the influence of the thermo-osmotic effects to the slip velocity is negligible.

The thermic influence in the bulk flow is more important. By taking into account this effect, a simple analytic relation for the neutral stability curves $k(\Delta V)$ was derived for $k = O(1)$, $\nu \to 0$, $\mathrm{Bi} \to 0$, and $\Delta V = O(\ln \nu)$,

$$1 = \frac{\varkappa}{8}\Delta V^2 \frac{k^3 \cosh k - \sinh^3 k}{4 \sinh k (k^2 - \sinh^2 k)} - \mathrm{Ra}\frac{\Delta V}{8}\mathrm{Bi}\frac{k^2(\sinh k - k\cosh k)^2 - (k^2 - \sinh^2 k)^2}{k^4 \sinh^2 k (k^2 - \sinh^2 k)}, \tag{38}$$

which qualitatively describes the influence of the thermal effects on the stability.

At $\mathrm{Ra} = 0$ this formula turns into the Rubinstein-Zaltzman relation (94) that is given in [29]. The second term on the right-hand side of (38), which is proportional to Ra, is responsible for the bulk thermal effects. The main conclusion from the formula described by Eq. (38) is that the system is destabilized by thermic effects for $\mathrm{Ra} < 0$ (heating from the top) and stabilized for $\mathrm{Ra} > 0$ (heating from the bottom). Note that the Rayleigh-Bénard convection only occurs in the opposite case when the liquid is heated from the bottom, $\mathrm{Ra} > 0$. [Changing the sign of Ra is equivalent to rotating the system at 180° relative to the direction of gravity (see Fig. 3).]

The eigenvalue stability problem is solved numerically using the method in [31]. The Galerkin pseudospectral τ method with Chebyshev polynomials taken as the basic functions is employed to discretize the eigenvalue problem (28)–(36). The generalized matrix eigenvalue problem is solved by the QR algorithm. There are up to 512 Chebyshev functions in the expansion.

The eigenvalues λ_j were real numbers in all of our calculations, which means that the instability is monotonic. These eigenvalues are arranged so that $\lambda_1 > \lambda_2 > \lambda_3 > \cdots$. Marginal stability curves are determined by the most dangerous eigenvalue $\lambda = \lambda_1$. Furthermore, we will only consider the most dangerous eigenvalue and hence we will skip subscript 1 in λ_1. Our numerical calculations confirm the main conclusion following from Eq. (38) of the destabilization of the 1D equilibria for negative Ra (heating from the top) and stabilization at positive Ra (heating from the bottom).

Figure 5 pictures the marginal stability curves, k versus ΔV at several values of Ra. The case of the pure electrokinetic instability $\mathrm{Ra} = 0$, which is a short-wave instability, separates the destabilizing and stabilizing effects of Joule heating. At $\mathrm{Ra} > 0$, the system is stabilized by thermic effects. For the case $\mathrm{Ra} < 0$, the system is destabilized with respect to long-wave perturbations. Further increasing the potential drop leads to instability intensification and an extension of the unstable wave-number range: Joule heating significantly changes the behavior of the instability. The Rayleigh-Bénard instability $\mathrm{Ra} > 0$ is connected with another eigenvalue of the spectrum and is not considered in the present work. Note only that this instability occurs at very large Rayleigh numbers $\mathrm{Ra} \approx 50\,000$, which is not realistic for membrane systems.

For $\mathrm{Ra} < 0$ in a small vicinity of the critical point $\Delta V = \Delta V^*$, the growth rate obeys the relation

$$\frac{1}{4}\frac{\lambda}{\lambda_m} = \left(\frac{k}{k_0}\right)^2 - \left(\frac{k}{k_0}\right)^4, \quad \lambda_m \sim \sqrt{\Delta V - \Delta V^*}, \tag{39}$$

which is a Taylor expansion of $\lambda(k)$ near $k = 0$. Here k_0 is a neutral wave number and $k_m = \frac{\sqrt{2}}{2}k_0$ is a wave number of the most dangerous mode with the maximum growth rate λ_m. The dispersion

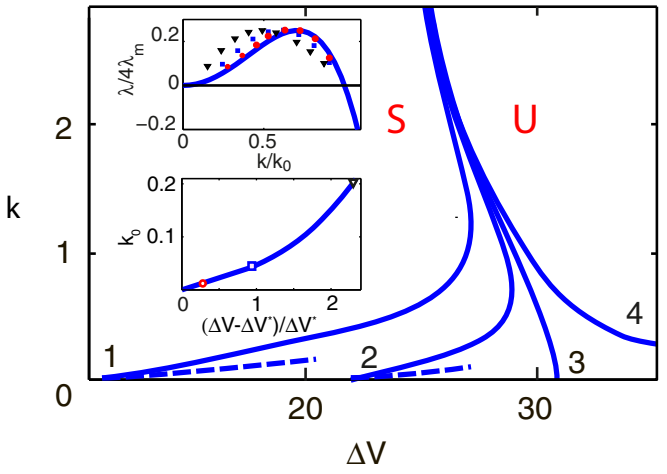

FIG. 5. Marginal stability curves of wave number k versus the potential drop ΔV for Ra $= -50$, curve 1; Ra $= -10$, curve 2; Ra $= 0$, curve 3; and Ra $= 10$, curve 4. The dashed line stands for the wave number of the most dangerous perturbations. The top inset shows $\lambda/4\lambda_m$ vs k/k_0 and the bottom inset shows k_0 versus $(\Delta V - \Delta V^*)/\Delta V^*$ for Ra $= -50$. Circles denote $\Delta V = 10$, squares $\Delta V = 15$, and triangles $\Delta V = 25$, taken from the numerical experiments.

relation (39) corresponds to the linear Kuramoto-Sivashinsky equation [53]

$$\frac{\partial H}{\partial \tau} + \frac{\partial^2 H}{\partial \xi^2} + \frac{\partial^4 H}{\partial \xi^4} = 0, \quad \xi = k_0 x, \quad \tau = \lambda_m t \tag{40}$$

for the 2D case and the linear Kuramoto-Sivashinsky equation

$$\frac{\partial H}{\partial \tau} + \nabla_s^2 H + \nabla_s^4 H = 0, \quad \zeta = k_0 z, \quad \nabla_s = \left(\frac{\partial}{\partial \xi}, \frac{\partial}{\partial \zeta}\right) \tag{41}$$

for the 3D case, which is in contrast to the complex Ginzburg-Landau equation for the short-wave electrokinetic instability [31] (see, for example, [53,54]).

The dependence of the normalized voltage $\Delta V^*/\Delta V_0^*$ (ΔV_0^* is a critical voltage at Ra $= 0$) on Ra is shown in Fig. 6(a). Here one can see the destabilizing thermal effect; that is, increasing |Ra|

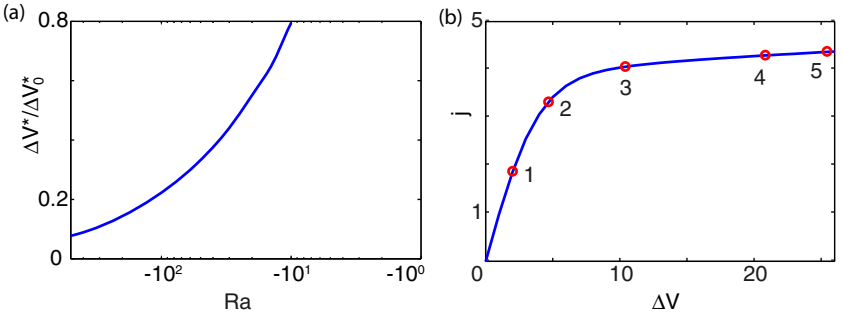

FIG. 6. (a) Dependence of the critical potential drop ΔV^* normalized to its value at Ra $= 0$ on the Rayleigh number. (b) The VC curve. Circles stand for the critical ΔV^* at different Rayleigh numbers: 1, Ra $= -500$; 2, Ra $= -150$; 3, Ra $= -50$; 4, Ra $= -10$; and 5, Ra $= -5$.

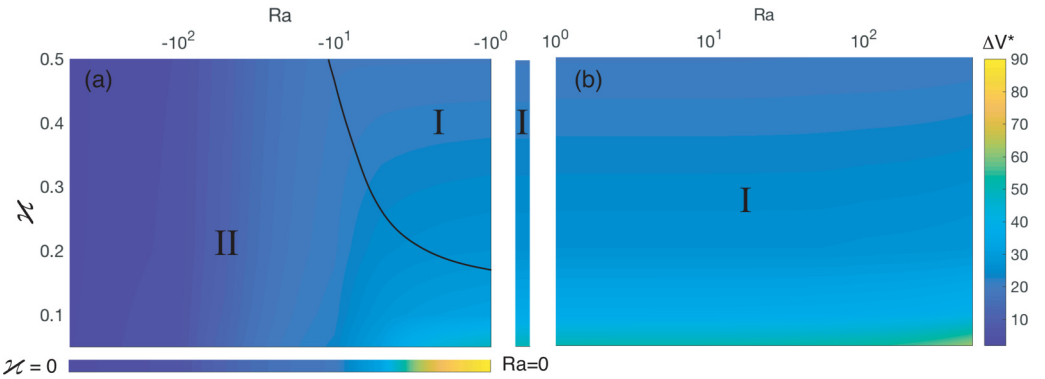

FIG. 7. Regions of domination of each mechanisms for (a) negative values of Ra and (b) positive values of Ra: I, electrokinetic instability region, and II, thermoelectrokinetic instability region. The color field on the background represents the critical voltage.

from 0 to 500 leads to a ten-times reduction of the threshold of instability. Because of this dramatic reduction, it is instructive to place the critical voltage on the VC characteristic [see Fig. 6(b)]. Recall that the critical point corresponds to the transition point to overlimiting regimes. Usually, transition to the overlimiting currents occurs at the limiting regimes (see [19,30–32,55]); see points 2–5 for relatively small |Ra|. It is interesting that for sufficiently large |Ra|, this transition takes place at the underlimiting currents, point 1. Such an unusual transition for the electrokinetic instability was recently found in [43,55]; for experimental evidence, see [27].

Regions of the domination of each mechanism (electrokinetic and thermoelectrokinetic instabilities) are shown in Fig. 7. The instability is long wave in the region thermoelectrokinetic domination and by crossing a boundary with electrokinetic region the instability changes to the short-wave electrokinetic instability. Implementation of a regime in the transition regions significantly depends on the wavelengths of the perturbations in the real physical systems.

B. Key mechanism of thermoelectrokinetic instability

The result that the quiescent 1D equilibrium is unstable for the negative Ra appears to be unexpected if we take into account the point that the upper arrangement of the maximum of temperature in the equilibrium state corresponds to the upper arrangement of the cathode (Fig. 3) and such a stratification is usually steady from the viewpoint of the Rayleigh-Bénard convection. When neglecting the electric forces ($\varkappa = 0$), the short-wave electrokinetic instability in the system disappears completely and only the long-wave thermal instability is retained [see Eq. (38)]. At $\varkappa = 0$, the buoyancy force proportional to the disturbance in the temperature $\hat{T}$ is the sole force in Eq. (3) of motion that is able to remove the system from the state of mechanical equilibrium. We recall the mechanism of occurrence of the Rayleigh-Bénard instability upon heating from below. We assume that a weak motion in the form of a circulating cell appears in the layer. Let the fluid velocity be directed upward in the left half of the cell and downward in the right half [Fig. 8(a)]. On the left, the fluid, which comes from the lower layers, is warmer and, correspondingly, lighter. On the right, coming from above, the fluid is colder and heavier. Consequently, the buoyancy force moment arises, which strengthens the motion. If the arising forces exceed the forces of viscous resistance, then the Rayleigh-Bénard convection begins. During heating from above, a convective motion is impossible in the classical case. The difference in the system under consideration from the classical case is the fact that the change in temperature at this point also occurs due to the change in the internal heat release, which is caused by the change in the electric current intensity determined by the total ion concentration K instead of only through the mechanism of convective heat transfer.

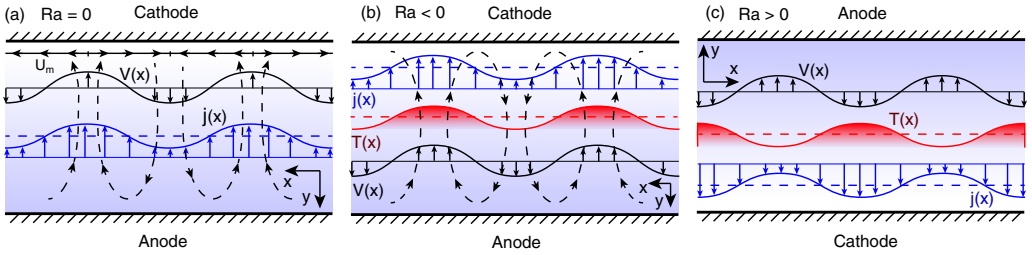

FIG. 8. (a) Schematic of the Rayleigh-Bénard convection at Ra $>$ 0, (b) thermoelectrokinetic destabilizing at Ra $<$ 0, and (c) thermoelectric stabilizing at Ra $>$ 0.

At the upper arrangement of the cathode (Ra $<$ 0), the total ion concentration K in the equilibrium state on most of the layer thickness increases from above down [see Fig. 8(b), where the point $y = 0$ corresponds to the upper boundary]. With the occurrence of motion, the convective ion transport leads to an increase in K for the fluid rise zone and to a decrease in K for the fluid descent zone in the right half of the cell [Fig. 8(b)]. As a result, in the left half of the cell, the current density j increases (and in the right half, it decreases), as does the Joule heat release, and with them, the temperature. By virtue of this situation, the disturbance of the temperature in the considered range of parameters of the problem proves to exceed by 2–3 orders of magnitude the disturbance opposite in sign associated with the convective heat transport; therefore, the instability arises. Following similar reasoning for the case of Ra $>$ 0 [Fig. 8(c)], we arrive at the conclusion that the arising moment of buoyancy forces operates against the disturbance of motion, which stabilizes the system.

C. Direct numerical simulation of the overlimiting regime

Let us consider the DNS of the full nonlinear NPPS system (8)–(15) with the natural white-noise initial conditions (17) and (18). The DNS of the system is implemented by applying the Galerkin pseudospectral τ method. A periodic domain along the membrane surface allows the utilization of the Fourier series $\exp(inkx)$ and $\exp(imkz)$ in the x and z directions, respectively. The Chebyshev polynomials are applied in the transverse direction y. The accumulation of the zeros of these polynomials near the walls allows us to properly resolve the thin ESC regions, $O(v)$.

Substituting the finite Fourier-Chebyshev series into the system (8)–(11) and using the Lanczos τ method (see [56]) to satisfy the BCs (13)–(15) leads to the system of coupled ordinary differential equations for the unknown Galerkin coefficients $c^{\pm}_{m,n}(t)$ and $T_{m,n}(t)$ and systems of linear algebraic equations with respect to $\Phi_{m,n}$, $U_{m,n}$, $V_{n,m}$, $W_{n,n}$, and $\Pi_{n,m}$. To obtain these systems, all nonlinear algebraic operations are executed in the physical space in the collocation points, while the derivatives with respect to both spatial variables x and z are calculated in the space of the Fourier coefficients. The derivatives of the Chebyshev polynomials are calculated by means of the collocation matrix method (see [56]). The connection between the collocation points and the Galerkin coefficients is performed by means of the fast Fourier transform.

A special method is developed to integrate the system in time. To continue the solution $c^{\pm}_{m,n}(t)$ and $T_{m,n}(t)$ from some time layer t to a new time layer $t + \Delta t$, a linear algebraic system with respect to the potential $\Phi_{n,m}$ corresponding to the Poisson equation should first be solved. Second, the velocity components $U_{n,m}$, $V_{n,m}$, and $W_{n,m}$ and pressure $\Pi_{n,m}$ from a linear algebraic system corresponding to the Stokes system are found. Third, the transport equations for the concentrations and the energy equation for the temperature are integrated and $c^{\pm}_{m,n}(t + \Delta t)$ and $T_{m,n}(t + \Delta t)$ are found. The second-order Adams-Bashforth scheme for nonlinear terms and the Crank-Nicolson scheme for linear terms are used.

A critical voltage ΔV^* (or critical Rayleigh number Ra*) acts as a threshold between the limiting (or underlimiting) 1D steady-state regimes and the 2D overlimiting regimes. For $\Delta V < \Delta V^*$, all

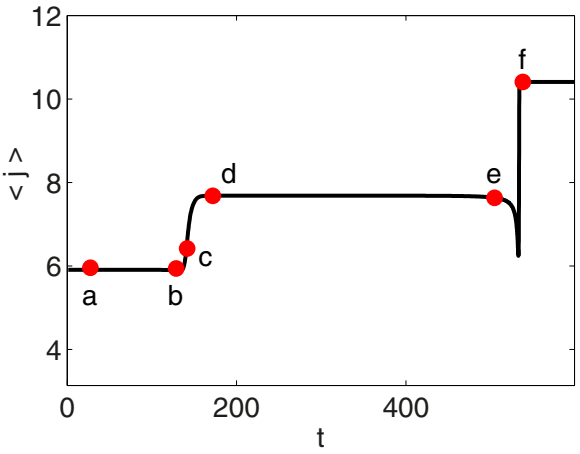

FIG. 9. Typical evolution of the average electric current $\langle j(t)\rangle$ from the initial room disturbances for the 2D regime. The parameters are $\mathrm{Ra} = -50$ and $\Delta V = 20$. Points on the curve correspond to a, $t = 10$; b, $t = 120$; c, $t = 150$; d, $t = 180$; e, $t = 500$, and f, $t = 530$.

of the imposed perturbations decay and eventually at $t \to \infty$ a previously found 1D equilibrium is realized. The case of the supercritical voltage $\Delta V > \Delta V^*$ is more interesting because the natural room disturbances will grow and eventually destroy the 1D equilibrium. For a small supercriticality, the 2D regimes are always realized, even for the 3D white-noise initial conditions and hence let us first consider the evolution of perturbations and the corresponding coherent structures for the 2D case.

A typical evolution of the averaged electric current $\langle j(t)\rangle$ is shown in Fig. 9. In contrast to the short-wave electrokinetic instability, the long-wave thermoelectrokinetic instability not only requires a much longer channel but also evolves much more slowly; the dimensional characteristic time to reach an attractor is about several hours. For the electrokinetic instability, this time is several tens of minutes (see [31]). Corresponding to the points a–e, the charge density distribution ρ is presented in Fig. 10. The darker regions in Fig. 10(f) correspond to the larger charge densities. Point a in the ESC region, which is characteristic of the limiting regimes, is already formed and one can see the charge maximum far from the wall. The time is small for the disturbances to manifest themselves and the solution is one dimensional. At the next stage of the evolution, the ESC region is clearly seen at point b. At this stage, the linear instability filters broadband initial noise into a sharp band near the wave number of the maximum growth rate. The boundary y_m between the ESC and the electroneutral region is nearly sinusoidal, with a wave number in good agreement with that found by the linear stability analysis. The amplitude of $\langle j\rangle$ between a and b is practically constant with respect to time. An unusual behavior can be seen between points b and d. The ESC region rapidly and dramatically changes in two different ways. First, a fraction of the space charge in the vicinity of the minimum of $y_m(x)$ transforms into a pattern that reminds us of antlers or a crown (we prefer to use the latter term). Second, rapid atomization of the rest fraction of the ESC region happens. The wavy arrows at point c show the process tendency and direction, while the charge fog in the bulk at point d manifests the result of this explosion. Note that there is a fast increase of the electric current $\langle j\rangle$ during this process. The initial distance between the crowns is determined by the linear maximum growth rate wave number but further on this distance changes and the final distance is subject to the nonlinearity of the system. The crowns are rather robust coherent structures and starting from point d they do not change their shape, but the fog eventually disappears and condenses and eventually its charge is accumulated in the EDLs on the wall (see point e). At this point, the localized coherent structures are surrounded by the EDLs. The charge in the neighboring EDLs is always different.

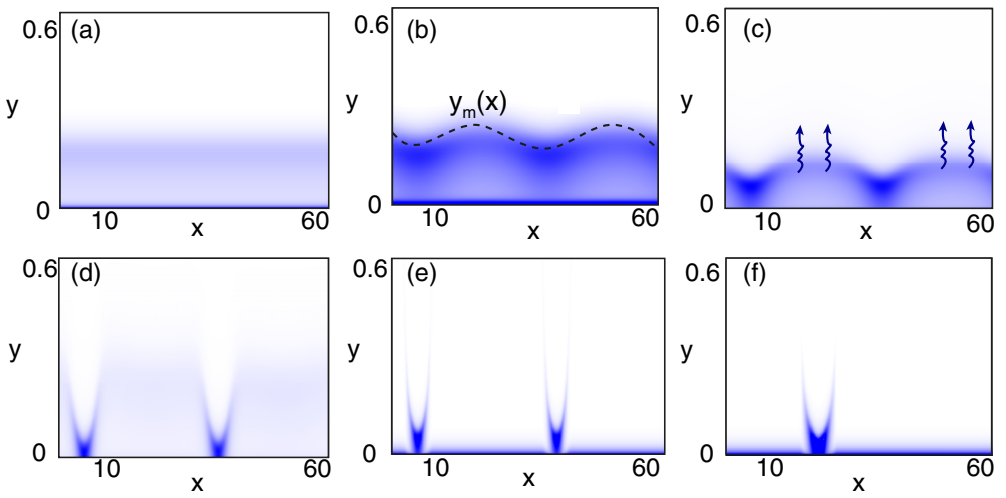

FIG. 10. Snapshots of the charge density $\rho(x,y,t)$ at different times. Darker regions correspond to larger charge densities. The parameters are Ra $= -50$, $\Delta V = 20$, and (a) $t = 10$, (b) $t = 120$, (c) $t = 150$, (d) $t = 180$, (e) $t = 500$, and (f) $t = 530$.

The charges of the same sign repel and the charge difference makes the crowns move towards each other with a final coalescence. The original number of crowns can be different and this depends on the length of the channel, but the final result is the same: Only one coherent structure survives. It takes a long time to reach this attractor and as the channel length increases it becomes longer. The process of fusion of the crowns is accompanied by a jump in the current, which increases after coalescence.

The steady 2D coherent structures of the charge distribution $\rho(x,y)$ for the electrokinetic (see [30–32]) and thermoelectrokinetic instabilities are compared in Fig. 11. In both cases, there is a rather sharp boundary $y_m(x)$ between the space charge and the electroneutral regions. Immediately, one can see a dramatic difference in the ρ distribution for these two types of instability. The electrokinetic structure has a spikelike shape where the regions of small charge in the spikes are joined by thin flat regions of large charge; the spikes inside are nearly empty (the charge density is small). A

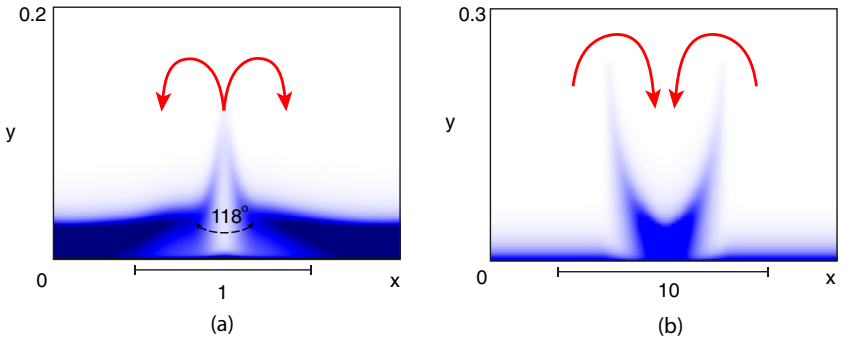

FIG. 11. Space charge distribution $\rho(x,y)$ for (a) the electrokinetic coherent structures having a spiked shape ($\Delta V = 30$ and Ra $= 0$) and (b) the thermoelectrokinetic structures forming crowns ($\Delta V = 30$ and Ra $= -50$). Liquid flow is shown schematically by the arrows. The bar stands for the characteristic width of the structures.

self-similar behavior was found in the vicinity of the spike apex. In particular, the apex angle is universal, about 118°, and it does not depend on the system parameters (see [57]). The space charge distribution on y at any fixed x has a maximum far from the wall and hence corresponds to the limiting currents. The characteristic size of the spike in the y direction is a small value $O(y_m)$ and dimensionally this size is up 1 μm. The spikes form either periodic structures or chaotic structures along the membrane. In both cases, the characteristic separation distance between the spikes and the spike width are about the distance between the upper and lower membranes. This follows from the short-wave type of electrokinetic instability (see [31]).

The coherent structure of the thermoelectrokinetic instability always has a crown shape with a large charge inside this crown and a relatively small charge in the neighboring flat regions. The characteristic size of the crown in the y direction is much larger than that of the spike and is varied from one-third to one-half of the distance between the membranes. At $t \to \infty$, after all the coalescences, only one crown survives and hence the characteristic length in the x direction depends on the channel length and is proportional to this length. The behavior of these coherent structures, particularly their coalescences, reminds us of solitary pulses in active media (see [54]). Note that, for short enough channels the thermoelectrokinetic structures do not exist because of a long-wave type of instability.

Our simulations [30–32] showed that for the electrokinetic coherent structures the liquid always flows upward from the cusp points of the ρ distribution and returns to the membrane surface, moving towards the flat regions of the ρ distribution (see the arrows in Fig. 11). Meanwhile, the direction is reversed for the thermoelectrokinetic coherent structures: The liquid always flows from the flat regions of the ρ distribution inward towards the crowns. These directions determine the shape of the microvortices in both cases.

To elucidate the properties of the thermoelectrokinetic coherent structures and to give a complete picture of their behavior, the fields of the charge density $\rho(x,y)$, the salt concentration $K(x,y)$, the temperature $T(x,y)$, and the stream function $\Psi(x,y)$, along with their representative dependences on y for fixed x, are presented in Fig. 12 for typical parameter values. Inside the crown, point 1, the ρ dependence on y has a typical limiting regime profile, with a maximum far from the wall. Outside the crown, neighboring the crown's flat regions, point 2, $\rho(y)$ has a monotonically decaying profile that is typical for the underlimiting currents [see Fig. 12(a)]. Hence, these neighboring regions are stable with respect to the secondary instability. The secondary instability of the flat neighboring spike regions is a peculiar feature of the electrokinetic mode; for the interpretation of the physical mechanism of the secondary instability see Fig. 9(b) in [30] and the discussion of this figure therein. The secondary instability is the main factor in bifurcations and the transition to chaotic behavior in the electrokinetic instability [see Fig. 10(b) herein and Fig. 14 in [31] and the corresponding text in the cited paper]. The absence of this secondary instability leads to a rather regular behavior for the thermoelectrokinetic mode, which is formation of a sole crown structure for the whole channel.

While the charge density $\rho(x,y)$ is located in the vicinity of the cathode $y = 0$, the salt concentration $K(x,y)$ descends from the anode $y = 1$ towards the cathode and it has a needle-type profile [see Fig. 12(b)]. Outside this narrow needle, the salt concentration is very small, practically zero, when compared to the salt distribution at points 1 and 2. The largest concentration within the needle region in some of our calculations reached a value as high as 500 of the initial concentration at $t = 0$ and we can talk about salt superconcentration similar to that found experimentally in other electrokinetic flows (see [1,58]). The electric conductivity is proportional to K and hence we can only expect a large electric current $j(x)$ in the vicinity of point 1. The electric current distribution along the membrane surface is shown in Fig. 13(a).

The temperature field $T(x,y)$ is shown in Fig. 12(c). This is caused by Joule heating and hence has maximum values in the same region as the salt concentration K and the electric current j. The largest temperature variation is seen in the x direction. On the background of this variation, change in the y direction is indistinguishable for the 2D field $T(x,y)$ but it is readily seen for fixed x at points 1 and 2.

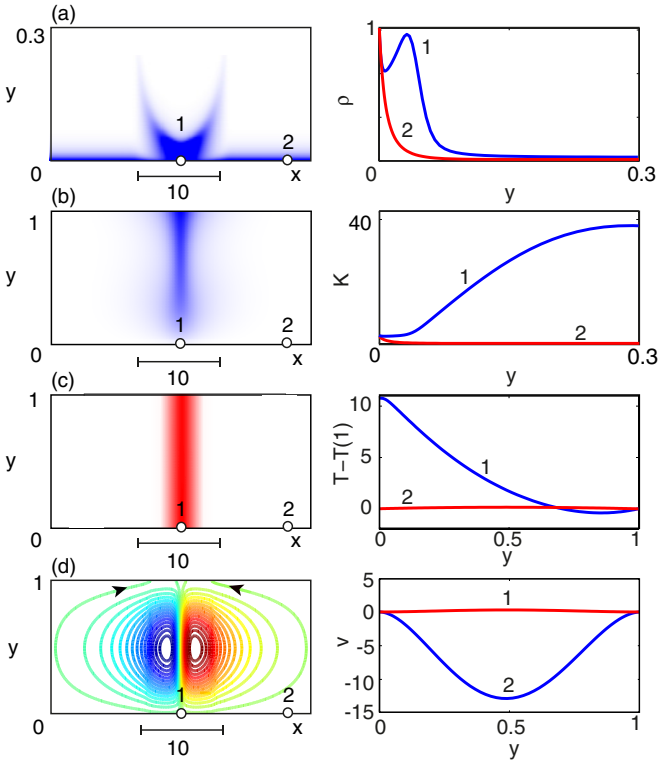

FIG. 12. Shown on the left are characteristic fields of typical steady-state 2D structures: (a) charge density $\rho(x,y)$, (b) salt concentration $K(x,y)$, (c) temperature $T(x,y)$, and (d) streamlines $\Psi(x,y)$. On the right are the cross sections of ρ, K, $T-T(1)$, and normal to the membrane surface velocity V at fixed $x=20$ (in the middle of the coherent structure) and $x=38$. The parameters are $\mathrm{Ra}=-50$ and $\Delta V=30$.

The development of the instability in the system leads to the formation of the microvortex motion. The streamlines of the flow are shown in Fig. 12(d). Liquid gushes up from the flat regions of the ρ distribution towards the upper membrane $y=1$ and returns to the lower membrane $y=0$ moving towards the crown and hence forms a pair of thermoelectroconvective vortices with their centers close to the center of the channel $y=1/2$. The vertical component of the velocity $V(y)$ is maximal in the center of the crown, point 1, symmetric with respect to the point $y=1/2$, and decays to practically zero far from the crown.

For a large enough supercriticality $\Delta V>\Delta V_{3D}>\Delta V^*$, the 2D coherent structures become unstable to 3D perturbations. The typical evolution of the electric current $\langle j(t)\rangle$ from the white-noise initial conditions at $t=0$, for this region of ΔV, is shown in Fig. 14.

To visualize the 3D fields of the unknowns during their evolution, it is convenient to use the $y_m(x,z)$ profiles. These profiles are presented in Fig. 15 for time points a–i of Fig. 14. The 3D circular coherent structures are formed after a short transition time, from point a to point b. For the first point, which is presented in Fig. 15(a), one can see a uniform charge distribution that corresponds to the 1D solution. The imposed small disturbances after a linear stage of their evolution, as described by the linear Kuramoto-Sivashinsky equation (41) (not shown in Fig. 15), evolve into the circular coherent structures of a small amplitude [Fig. 15(b)]. Their amplitude increases with time and at the same time new circular coherent structures are generated, points c and d. At the last point, point d, a well-developed system of the coherent structures' regular distribution is formed. Note that they are distributed in space and not in the usual checkerboard order but in a rectangular order.

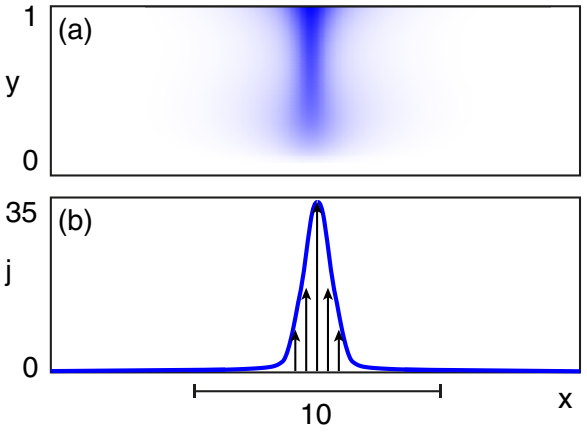

FIG. 13. (a) Salt concentration $K(x,y)$ and (b) electric current j. The parameters are $\mathrm{Ra} = -50$ and $\Delta V = 30$.

The small asymmetry of the pattern location and hence small asymmetry of charge in the neighboring regions is the reason for a net Coulomb force that moves the crowns towards each other. The mechanism here is rather similar to that of the 2D structures [see Fig. 10(h)]. The arrows in Fig. 15 show the direction of this movement, which results in the structures' coalescence and the following coarsening of their distribution (reducing the number of patterns). Either a paired coalescence [see Figs. 15(d)–15(f)] or a quadruple coalescence [see Fig. 15(g)] takes place. The final result is the same as for the 2D regime: Only one coherent structure survives; a longer and wider channel will make it longer to reach this attractor. Another feature that is similar to the 2D evolution is that upon each coalescence, there is a jump of $\langle j(t)\rangle$. The first jump, from point a to d, is as much as three times larger than that for the 2D regime, while all of the other jumps are weaker. Note that between points d and e there is a rapid movement of the charge from the ESC region into

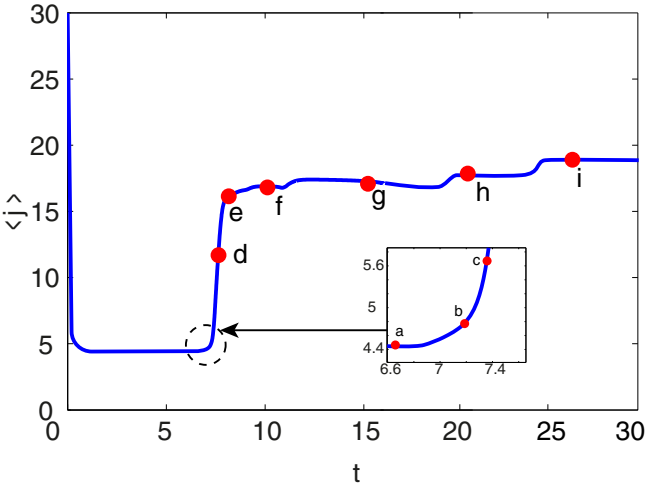

FIG. 14. Typical evolution of the average electric current $\langle j(t)\rangle$ from the initial room disturbances for the 3D regime. The parameters are $\mathrm{Ra} = -50$ and $\Delta V = 35$. Points on the curve correspond to a, $t = 6.63$; b, $t = 7.2$; c, $t = 7.4$; d, $t = 8$; e, $t = 8.9$; f, $t = 11$; g, $t = 15.3$; h, $t = 21$; and i, $t = 27$.

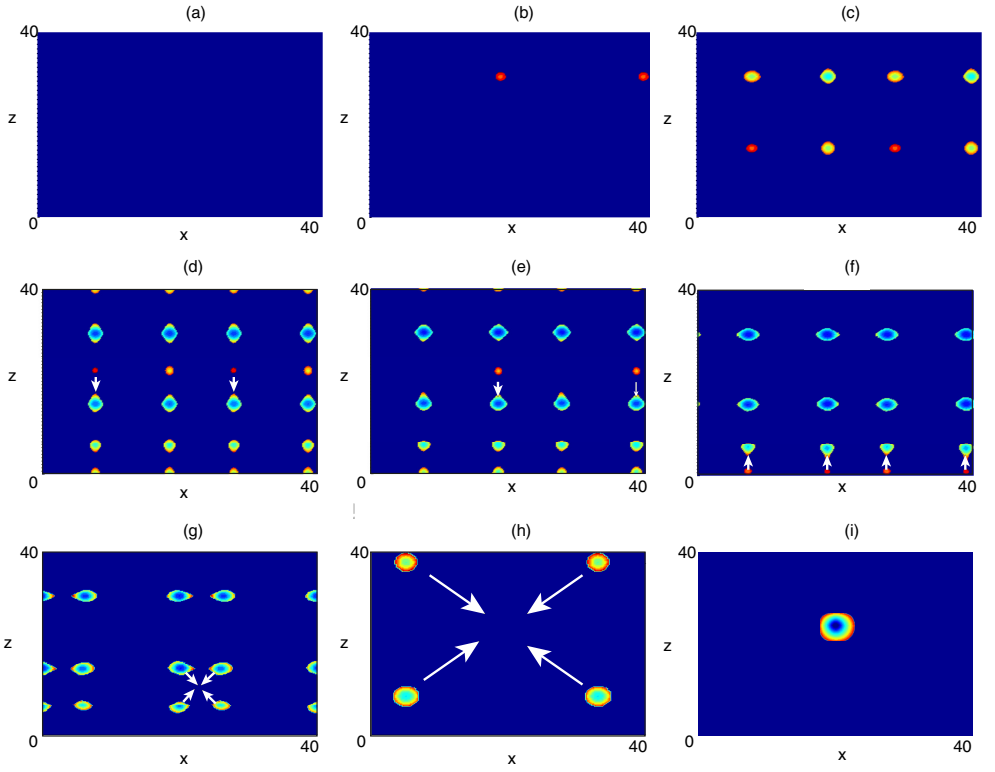

FIG. 15. Snapshots of $y_m(x,y,)$ at different times. The parameters are $\mathrm{Ra} = -50$, $\Delta V = 35$, and (a) $t = 6.63$, (b) $t = 7.2$, (c) $t = 7.4$, (d) $t = 8$, (e) $t = 8.9$, (f) $t = 11$, (g) $t = 15.3$, (h) $t = 21$, and (i) $t = 27$.

the electroneutral bulk, following charge atomization and its final condensation to the ESC region. This phenomenon is qualitatively similar to its 2D analog.

Steady 3D coherent structures of $y = y_m(x,z)$ for the electrokinetic (see [32]) and thermoelectrokinetic instabilities are compared in Fig. 16. The electrokinetic structure looks like a hexagon. The $y_m(x,z)$ profile consists of six wedgelike lateral faces and six pyramids are located at their intersection. In the remaining area, $y_m(x,z)$ is flat and situated in lowlands. The angle of the faces

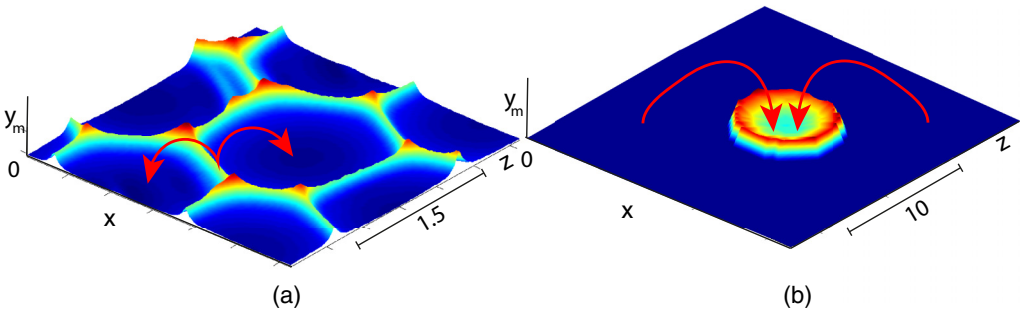

FIG. 16. Comparison of the typical 3D coherent structures for (a) the electrokinetic instability and (b) the thermoelectrokinetic instability. The arrows schematically show the direction of the liquid flow. The parameters are $\Delta V = 50$ for the electrokinetic instability and $\mathrm{Ra} = -50$ and $\Delta V = 35$ for the thermoelectrokinetic instability.

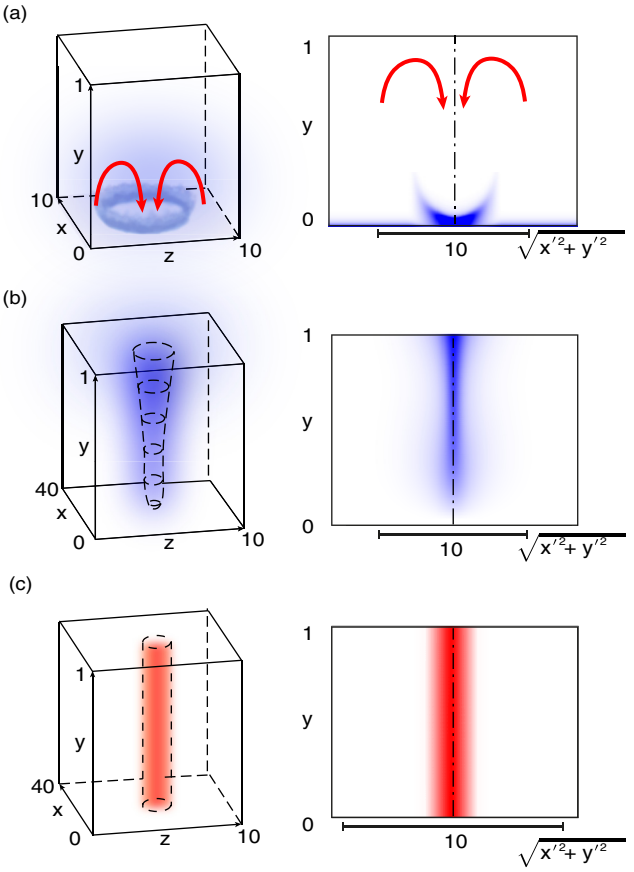

FIG. 17. Shown on the left are fields of the 3D coherent structures for (a) the charge density $\rho(x,y,z)$, (b) the salt concentration $K(x,y,z)$, and (c) the temperature $T(x,y,z)$. On the right are their 2D cross sections at $\Delta V = 35$ and $\mathrm{Ra} = -50$.

is close to that for the 2D spikes, 118°. A rough evaluation of the pyramidal angle gives its value as about 80°–90°. This angle is nearly independent of the parameters of the system. As for the 2D case, a self-similar behavior was found in the vicinity of the pyramid apex. In particular, the apex angle is universal, 77° (see [57]). The flat lowlands of y_m contain a large charge and in the maximums of y_m the charge density is minimal. The liquid always flows upward from the cusp points of the y_m distribution and returns to the membrane surface, moving towards the flat regions of the y_m distribution. An array of vortex pairs is formed, which is schematically shown in Fig. 16 by the arrows. Is is worthwhile mentioning that as the voltage ΔV increases, the regular steady-state hexagonal patterns break down into complex and highly disordered states of spatiotemporal chaos.

The coherent structure of the thermoelectrokinetic instability is much simpler. We have not observed a chaotic behavior in any of our calculations, either for the 2D regime or for the 3D regime: The final stage was always one steady-state circular coherent structure [see Fig. 16(b)]. Outside the structure, the $y_m(x,z)$ distribution is flat and situated in the lowlands. The characteristic size of this pattern along the membrane, in the x and z directions, as well as normally to the membrane in the y direction, is much larger than for the electrokinetic hexagon. As for the 2D case, the characteristic size along the membrane is proportional to the channel length and width. There is a large charge inside the localized thermoelectrokinetic pattern and a small charge in the flat neighboring region. For the thermoelectrokinetic patterns, the liquid always flows from the flat regions of the y_m distribution

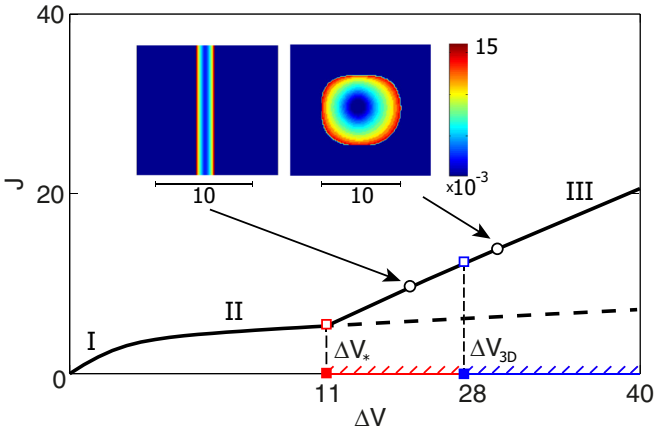

FIG. 18. Typical VC characteristic for Ra $= -50$. Here I, II, and III stand for underlimiting, limiting, and overlimiting currents, respectively. The solid line corresponds to our 3D simulations and the dashed line corresponds to the 1D solution. The inset shows two typical thermoelectrokinetic patterns for y_m: the 2D thermoelectroconvective roll and the regular 3D circle structure.

inward to the coherent structure [see the arrows in Fig. 16(b)]. Eventually, a circular microvortex flow is formed.

The typical field distribution of the charge density $\rho(x,y,z)$, the salt concentration $K(x,y,z)$, and the temperature $T(x,y,z)$ is presented in Fig. 17 together with their cross sections. The charge density forms an axisymmetric circular structure in the vicinity of the membrane surface $y = 0$. The maximum charge density is located inside the crown. The charge density is small outside the crown and it is uniformly disturbed over x and z coordinates.

The salt concentration K descends from the anode at $y = 1$ towards the cathode and it forms a narrow stalactite-type profile. In some of our calculations, the salt concentration inside the stalactite reached a value of hundreds of the initial concentration at $t = 0$ and we can talk about superconcentration. Outside this narrow stalactite, the concentration is practically zero. This causes a large electric current j and a large Joule heating in the narrow salt "cord" The temperature field is shown in Fig. 17(c). In summary, we can say that 3D coherent structures and their fields qualitatively coincide with their 2D analogs.

The current distribution along the membrane has a maximum at the same location of x and z as the salt concentration. As we mentioned previously, in the 3D case the salt concentration has a stalactite form and it is more narrow than for the 2D case.

The dependence of the potential drop ΔV of the average electric current J over the membrane surface and the elapsed time [see Eq. (20)] complements our understanding of the system behavior. Such a VC dependence is shown in Fig. 18 for typical values of Ra, $\varkappa$, ν, and Bi. Portions of the VC dependence I, II, and III stand for the underlimiting, limiting, and overlimiting currents, respectively. The dashed line in Fig. 18 stands for the unstable underlimiting regimes. The bifurcation points of the 1D-2D and 2D-3D transitions, $\Delta V^* \approx 11$ and $\Delta V_{3D} \approx 28$, are designated by squares. For a small supercriticality the instability is two dimensional and for a sufficiently large supercriticality it is three dimensional. Our simulations show that only two basic coherent structures can be found during the evolution: the 2D and the 3D steady thermoelectrokinetic crowns of the charge density, stalactites of the salt concentration, and the corresponding microvortices. To complete the VC dependence, the y_m distribution is shown in the insets above the VC curve. The arrows show the place of these structures along the VC curve and there is a typical potential drop for their realization.

The results of the nonlinear investigation are generalized for several values of Ra in the VC characteristic curve presented in Fig. 19. The overlimiting current regimes start at the points predicted

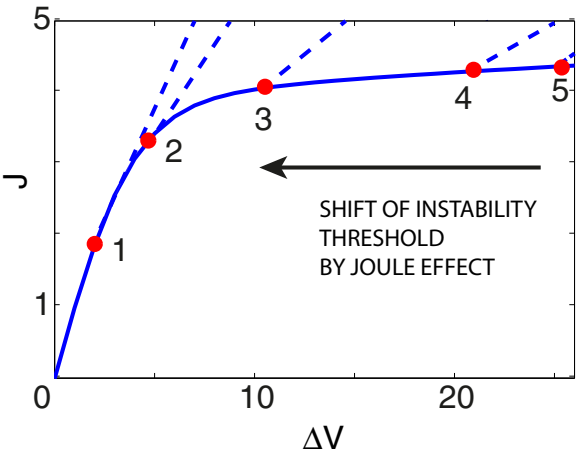

FIG. 19. Volt-current characteristics at different Rayleigh numbers: 1, Ra $= -500$; 2, Ra $= -150$; 3, Ra $= -50$; 4, Ra $= -10$; and 5, Ra $= -5$.

by the linear stability analysis. In the window Ra $= -500$ to Ra $= -150$, there is a transition from the underlimiting regime to the overlimiting one, bypassing the limiting regime.

IV. MAIN RESULTS AND CONCLUSIONS

An instability in an electrolyte solution near ion-selective surfaces in an external electric field was discovered and investigated numerically using parallel computing on the SKIF MSU Lomonosov supercomputer. While the mechanism of the instability is connected with Joule heating, it dramatically differs from the Raleigh-Bénard convection: The instability is caused by the nonuniformity of the electric current and the electric conductivity. The thermoelectrokinetic instability prevails in long microchannels and a good enough thermal insulation of the system and is an additional factor for the overlimiting current mode.

While noise initial conditions were taken to mimic room disturbances, they evolve towards rather unusual coherent structures. For the cation-exchange membranes, the salt concentration was eventually localized in narrow long fingers, which remind us of stalactites, and stretched from the anode in the direction of the cathode. Outside the stalactites, the salt concentration was practically zero, while inside the stalactites it could reach hundreds from the initial concentration. Thus, it is possible to talk about its superconcentration. The electric current propagates in a narrow needle along the stalactite with maximal electric conductivity and it gives rise to Joule heating in this region. The space charge forms crownlike micropatterns near the cathode. Note that the regime of chaotic motion that is characteristic of electrokinetic instability was not observed for the thermoelectrokinetic instability.

ACKNOWLEDGMENTS

E.N.K., E.A.D., G.S.G., and N.Y.G. were supported, in part, by the Russian Foundation for Basic Research (Projects No. 14-08-00789-a, No. 15-08-02483-a, No. 16-48-230107-r_a, and No. 16-08-00643-a). The research is carried out using the equipment of the shared research facilities of HPC computing resources at Lomonosov Moscow State University.

[1] Y.-C Wang, A. L. Stevens, and J. Han, Million-fold preconcentration of proteins and peptides by nanofluidic filter, Anal. Chem. **77**, 4293 (2005).

[2] R. B. Schoch, J. Han, and P. Renaud, Transport phenomena in nanofluidics, Rev. Mod. Phys. **80**, 839 (2008).
[3] V. V. Nikonenko, N. D. Pismenskaya, E. I. Belova, P. Sistat, P. Huguet, G. Pourcelly, and C. Larchet, Intensive current transfer in membrane systems: Modelling, mechanisms and application in electrodialysis, Adv. Colloid Interface Sci. **160**, 101 (2010).
[4] S. J. Kim, S. H. Ko, K. H. Kang, and J. Han, Direct seawater desalination by ion concentration polarization, Nat. Nanotech. **5**, 297 (2010).
[5] T. A. Zangle, A. Mani, and J. G. Santiago, Theory and experiments of concentration polarization and ion focusing at microchannel and nanochannel interfaces, Chem. Soc. Rev. **39**, 1014 (2010).
[6] A. Mani and M. Z. Bazant, Deionization shocks in microstructures, Phys. Rev. E **84**, 061504 (2011).
[7] M. E. Suss, T. F. Baumann, W. L. Bourcier, C. M. Spadaccini, K. A. Rose, J. G. Santiago, and M. Stadermann, Capacitive desalination with flow-through electrodes, Energy Environ. Sci. **5**, 9511 (2012).
[8] H.-C. Chang, G. Yossifon, and E. A. Demekhin, Nanoscale electrokinetics and microvortices: How microhydrodynamics affects nanofluidic ion flux, Annu. Rev. Fluid Mech. **44**, 401 (2012).
[9] V. V. Nikonenko, A. V. Kovalenko, M. K. Urtenov, N. D. Pismenskaya, J. Han, P. Sistat, and G. Pourcelly, Desalination at overlimiting currents: State-of-the-art and perspectives, Desalination **342**, 85 (2014).
[10] R. Kwak, G. Guan, W. K. Peng, and J. Han, Microscale electrodialysis: Concentration profiling and vortex visualization, Desalination **308**, 138 (2013).
[11] R. Kwak, V. S. Pham, K. M. Lim, and J. Han, Shear Flow of an Electrically Charged Fluid by Ion Concentration Polarization: Scaling Laws for Electroconvective Vortices, Phys. Rev. Lett. **110**, 114501 (2013).
[12] D. Deng, W. Aouad, W. A. Braff, S. Schlumpberger, M. E. Suss, and M. Z. Bazant, Water purification by shock electrodialysis: Deionization, filtration, separation, and disinfection, Desalination **357**, 77 (2015).
[13] V. G. Levich, *Physicochemical Hydrodynamics* (Prentice Hall, Englewood Cliffs, 1962).
[14] R. F. Probstein, *Physicochemical Hydrodynamics*, *An Introduction* (Wiley-Interscience, New York, 2005).
[15] I. Rubinstein and L. Shtilman, Voltage against current curves of cation exchange membranes, J. Chem. Soc. Faraday Trans. 2 **75**, 231 (1979).
[16] J. Balster, M. H. Yildirim, D. F. Stamatialis, R. Ibanez, R. G. H. Lammertink, V. Jordan, and M. Wessling, Morphology and microtopology of cation-exchange polymers and the origin of the overlimiting current, J. Phys. Chem. B **111**, 2152 (2007).
[17] V. I. Zabolotsky, V. V. Nikonenko, N. D. Pismenskaya, E. V. Laktionov, M. K. Urtenov, H. Strathmann, M. Wessling, and G. H. Koops, Coupled transport phenomena in overlimiting current electrodialysis, Sep. Purif. Technol. **14**, 255 (1998).
[18] E. I. Belova, G. Y. Lopatkova, N. D. Pismenskaya, V. V. Nikonenko, C. Larchet, and G. Pourcelly, Effect of anion-exchange membrane surface properties on mechanisms of overlimiting mass transfer, J. Phys. Chem. B **110**, 13458 (2006).
[19] B. Zaltzman and I. Rubinstein, Electro-osmotic slip and electroconvective instability, J. Fluid Mech. **579**, 173 (2007).
[20] V. A. Shaposhnik, V. I. Vasil'eva, and O. V. Grigorchuk, The interferometric investigations of electromembrane processes, Adv. Colloid Interface Sci. **139**, 74 (2008).
[21] N. D. Pismenskaya, V. V. Nikonenko, E. I. Belova, G. Y. Lopatkova, P. Sistat, G. Pourcelly, and K. Larshe, Coupled convection of solution near the surface of ion-exchange membranes in intensive current regimes, Russ. J. Electrochem. **43**, 307 (2007).
[22] Y. Kharkats, Mechanism of "supralimiting" currents at ion-exchange membrane/electrolyte interfaces. Sov. Electrochem. **21**, 917 (1985).
[23] H.-C. Chang, E. A. Demekhin, and V. S. Shelistov, Competition between Dukhin's and Rubinstein's electrokinetic modes, Phys. Rev. E **86**, 046319 (2012).
[24] S. M. Davidson, M. Wessling, and A. Mani, On the dynamical regimes of pattern-accelerated electroconvection, Sci. Rep. **6**, 22505 (2016).
[25] V. A. Kirii, V. S. Shelistov, and E. A. Demekhin, Hydrodynamics of spatially inhomogeneous real membranes, J. Appl. Mech. Tech. Phys. **58**, 635 (2017).

[26] V. A. Kiriy, V. S. Shelistov, E. N. Kalaidin, and E. A. Demekhin, Hydrodynamics, electroosmosis, and electrokinetic instability in imperfect electric membranes, Dokl. Phys. **62**, 222 (2017).
[27] E. D. Belashova, N. A. Melnik, N. D. Pismenskaya, K. A. Shestova, A. V. Nebavky, K. A. Lebedev, and V. V. Nikonenko, Overlimiting mass transfer through cation-exchange membranes modified by nafion film and carbon nanotubes, Electrochim. Acta **59**, 412 (2012).
[28] V. S. Shelistov, E. A. Demekhin, and G. S. Ganchenko, Electrokinetic instability near charge-selective hydrophobic surfaces, Phys. Rev. E **90**, 013001 (2014).
[29] I. Rubinstein and B. Zaltzman, Electro-osmotically induced convection at a permselective membrane, Phys. Rev. E **62**, 2238 (2000).
[30] E. A. Demekhin, V. S. Shelistov, and S. V. Polyanskikh, Linear and nonlinear evolution and diffusion layer selection in electrokinetic instability, Phys. Rev. E **84**, 036318 (2011).
[31] E. A. Demekhin, N. V. Nikitin, and V. S. Shelistov, Direct numerical simulation of electrokinetic instability and transition to chaotic motion, Phys. Fluids **25**, 122001 (2013).
[32] E. A. Demekhin, N. V. Nikitin, and V. S. Shelistov, Three-dimensional coherent structures of electrokinetic instability, Phys. Rev. E **90**, 013031 (2014).
[33] V. S. Pham, Z. Li, K. M. Lim, J. K. White, and J. Han, Direct numerical simulation of electroconvective instability and hysteretic current-voltage response of a permselective membrane, Phys. Rev. E **86**, 046310 (2012).
[34] C. L. Druzgalski, M. B. Andersen, and A. Mani, Direct numerical simulation of electroconvective instability and hydrodynamic chaos near an ion-selective surface, Phys. Fluids **25**, 110804 (2013).
[35] A. T. Pérez and A. Castellanos, Role of charge diffusion in finite-amplitude electroconvection, Phys. Rev. A **40**, 5844 (1989).
[36] I. Rubinstein, Electroconvection at an electrically inhomogeneous permselective interface, Phys. Fluids A **3**, 2301 (1991).
[37] I. Rehberg, F. Horner, and G. Hartung, The measurement of subcritical electroconvection, J. Stat. Phys. **64**, 1017 (1991).
[38] J. D. Posner and J. G. Santiago, Convective instability of electrokinetic flows in a cross-shaped microchannel, J. Fluid Mech. **555**, 1 (2006).
[39] E. Karatay, M. B. Andersen, M. Wessling, and A. Mani, Coupling Between Buoyancy Forces and Electroconvective Instability near Ion-Selective Surfaces, Phys. Rev. Lett. **116**, 194501 (2016).
[40] J. C. de Valenca, A. Kurniawan, R. M. Wagterveld, J. A. Wood, and R. G. H. Lammertink, Influence of Rayleigh-Bénard convection on electrokinetic instability in overlimiting current conditions, Phys. Rev. Fluids **2**, 033701 (2017).
[41] W. M. Saslow, Joule heating rate need not equal I^2R, where R is the Ohmic resistance: The case of voltaic cells, Phys. Rev. E **59**, R1343 (1999).
[42] R. Dey, T. Ghonge, and S. Chakraborty, Steric-effect-induced alteration of thermal transport phenomenon for mixed electroosmotic and pressure driven flows through narrow confinements, Int. J. Heat Mass Transfer **56**, 251 (2013).
[43] E. A. Demekhin, S. Amiroudine, G. S. Ganchenko, and N. Y. Khasmatulina, Thermoelectroconvection near charge-selective surfaces, Phys. Rev. E **91**, 063006 (2015).
[44] R. abu Rjal, L. Prigozhin, I. Rubinstein, and B. Zaltzman, Equilibrium electro-convective instability in concentration polarization: The effect of non-equal ionic diffusivities and longitudinal flow, Russ. J. Electrochem. **53**, 903 (2017).
[45] C. Soret, Sur l'état d'équilibre que prend au point de vue de sa concentration une dissolution saline primitivement homohéne dont deux parties sont portées á des temprétures différentes, Arch. Sci. Phys. Nat. **2**, 48 (1879).
[46] A. Würger, Transport in Charged Colloids Driven by Thermoelectricity, Phys. Rev. Lett. **101**, 108302 (2008).
[47] I. Chikina, V. Shikin, and A. A. Varlamov, Seebeck effect in electrolytes, Phys. Rev. E **86**, 011505 (2012).
[48] R. F. Stout and A. S. Khair, Diffuse charge dynamics in ionic thermoelectrochemical systems, Phys. Rev. E **96**, 022604 (2017).
[49] *CRC Handbook of Chemistry and Physics*, edited by D. Lide (CRC, New York, 1994).

[50] Z. R. Garnon and H.-C. Chang, Electrothermal ac electro-osmosis, Appl. Phys. Lett. **94**, 024101 (2009).
[51] P. Garcia-Sanchez, A. Ramos, and F. Mugele, Electrothermally driven flows in ac electrowetting, Phys. Rev. E **81**, 015303 (2010).
[52] I. Rubinstein and B. Zaltzman, Wave number selection in a nonequilibrium electro-osmotic instability, Phys. Rev. E **68**, 032501 (2003).
[53] M. C. Cross and P. C. Hohenberg, Pattern formation outside of equilibrium, Rev. Mod. Phys. **65**, 851 (1993).
[54] H.-C. Chang and E. A. Demekhin, *Complex Wave Dynamics on Thin Films* (Elsevier, Amsterdam, 2002), Vol. 14 .
[55] I. Rubinstein and B. Zaltzman, Equilibrium Electroconvective Instability, Phys. Rev. Lett. **114**, 114502 (2015).
[56] C. Canuto, M. Y. Hussaini, A. Quarteroni, and T. A. Zang, *Spectral Methods in Fluid Dynamics* (Springer, Berlin, 1987), p. 556.
[57] V. S. Shelistov, E. A. Demekhin, and G. S. Ganchenko, Self-similar solution to the problem of electrokinetic instability in semipermeable membranes, Moscow Univ. Mech. Bull. **69**, 119 (2014).
[58] S. C. Wang, H. H. Wei, H. P. Chen, M. H. Tsai, C. C. Yu, and H.-C. Chang, Dynamic superconcentration at critical-point double-layer gates of conducting nanoporous granules due to asymmetric tangential fluxes, Biomicrofluidics **2**, 014102 (2008).